ARTICLE

A spectIR-fluidic reactor for monitoring fast chemical reaction kinetics with on-chip attenuated total reflection Fourier transform infrared spectroscopy

Nan Jia,[a] Leon Torres de Oliveira,[a] André Bégin-Drolet[b] and Jesse Greener [a,c*]

Microfluidics has emerged as a powerful technology with diverse applications in microbiology, medicine, chemistry, and physics. While its potential for controlling and studying chemical reactions is well recognized, the extraction and utilization of the vast amounts of high-quality information generated within microfluidic devices remain challenging. This is mainly due to the limited tools available for *in situ* measurements of chemical reactions. In this study, we present a proof-of-concept spectIR-fluidic reactor design that combines microfluidics with Fourier transform infrared (FTIR) spectroscopy for *in situ* kinetic studies of fast reactions. By integrating a multi-ridge silicon attenuated total reflection (ATR) wafer into the microfluidic device, we enable multi-point measurements for precise reaction time monitoring. This work establishes a validated foundation for studying a wide range of chemical reactions using ATR-FTIR spectroscopy, which will enable simultaneous quantification of reagents, intermediates, and products. The spectIR-fluidic platform offers customizable designs, allowing for the investigation of reactions with various time scales, and has the potential to significantly advance reaction optimization and pathway exploration.

Introduction

Microfluidics is a rapidly developing technology with current and potential impact in research areas, including microbiology, medicine, chemistry and physics.[1] The domain has grown thanks to continuous technical developments,[2] and the growth of important applications, such as organ-on-a-chip,[3] microscale bioreactors,[4] bioanalytical lab-on-a-chip,[5] and point of care devices,[6] though challenges still exist.[7] One of the major advantages of microfluidics is the ability to control chemical processes via precise timing of reactions[8] and the accurate determination of temperature, concentration and other relevant reaction parameters.[9] These advantages can be especially important for kinetic studies.[10] The potential to leverage these amiable microfluidic qualities to control and study chemical reactions[11] has been a long-standing goal for the field, but the challenge in extraction and utilization of the vast amounts of high-quality information generated inside the device remains to this day.[12]

Kinetic studies in macro-flow systems are typically conducted by measuring the state of the reaction at different locations along the downstream path of the flow reactor. With the knowledge of the flow velocity, reaction kinetics can be studied using a so-called distance to time transformation.[13] This is advantageous over stop-flow experiments because the time of reaction is strictly related to measurement position, irrespective of the data acquisition time. Multi-point measurements are also preferred over fixed position measurements using variable flow rates to modulate the time due to corresponding changes in mixing and shear stress which can change the character of the reaction, especially for wall-adhered catalytic reactions in small channels. In microchannels, small dimensions result in fast flow velocities, which translates to high time resolution for kinetic measurements. This can play a crucial role in determining kinetic parameters and gaining insights into the underlying molecular processes that govern the reaction based on typical methods for initial rates. High time resolution reaction kinetics is especially important for systems that rapidly change in concentration (e.g., highly reactive/catalytic systems) and those which produce short-lived intermediates. Thus, broadly accessible microfluidic kinetic measurements can be crucial to help optimize reaction conditions and design new catalysts, and ultimately improve reaction efficiency.

A major bottle-neck for on-chip kinetic studies is the limited available tools available for *in situ* measurements of chemical reactions.[14] The small inaccessible analyte volumes inside microchannels limits traditional methods of chemical analysis even for fixed-point measurements. One approach to circumvent this limitation is to use the microfluidic reactor to prepare and time the reaction and then to make measurements after quenching or after rapid injection into a downstream analytical instrument. Some examples of such a hyphenated approach include the use of high-pressure liquid chromatography,[15] mass spectrometry,[13,16] UV-Vis spectroscopy,[17] and others.[18] Generally, time resolution in this approach is relatively slow and may not take advantage of the

[a.] *Département de chimie, Faculté des sciences et de génie, Université Laval, Québec, QC G1V 0A6, Canada.*
[b.] *Département de génie mécanique, Faculté des sciences et de génie, Université Laval, Québec, QC G1V 0A6, Canada.*
[c.] *CHU de Québec, centre de recherche du CHU de Québec, Université Laval, Québec, QC G1L 3L5, Canada*
* Corresponding author: Jesse.Greener@chm.ulaval.ca
Electronic Supplementary Information (ESI) available: See DOI: 10.1039/x0xx00000x

ability of microfluidic reactors to prepare reactions with high precision in time. Other limitations include complex interfacing and coordination between data acquisition and setting experimental conditions. Optical imaging through transparent microfluidic devices dominates as characterization tools,[19] and is compatible with multi-point measurements for kinetic studies, but generally it is not appropriate to monitor chemical reactions except for some multiphase reactions,[20,21] or those that which consume or produce light absorbing or emitting compounds.[22] Other more experimental techniques, such as time-resolved cryo-electron microscopy of single particles have been recently used to address kinetic questions related to the determination of structures of biological marcromolecules.[23]

Fourier transform infrared (FTIR) spectroscopy is an ideal modality for chemical detection because it can generate characteristic spectra for most materials[24] and is amenable to quantitative studies of the state of a chemical reaction for kinetic studies.[25] A major drawback is that infrared light is strongly absorbed by most materials, including polymers used in microfabrication of microchannels. It can also be completely attenuated by most solvents used for reaction chemistry after traveling through just a few microns.[26] While transmission mode is, therefore, untenable for most applications, attenuated total reflection (ATR) elements have been demonstrated as an avenue to combining microfluidics and FTIR. The technique is based on the interaction between the analyte fluid and the IR electromagnetic field which is trapped at the ATR crystal surface in the form of an IR evanescent wave. As such, direct IR-coupled reactions can be achieved without contacting device fabrication material, as demonstrated elsewhere.[27] This approach also limits the interaction between the probe field and analyte solution due to strong limits on evanescent field penetration depths, for example being sub-micron for germanium and silicon ATR crystals. However, making required multi-position measurements for kinetic studies may not be straightforward, which led to some early demonstrations of on-chip FTIR being driven by single-point approaches.[28] Exciting examples of multi-point ATR-FTIR measurements in microchannels have been demonstrated, but often require sacrifices to the microfluidic device and/or extensive analytical setups, including imaging detectors or highly focused displaceable beams, such as those from a synchrotron or quantum cascade lasers (QCL).[27,29]

Recently, we have demonstrated a versatile microfabrication approach called spectIR-fluidics, for the integration of a multi-ridge silicon ATR wafer (Si-ATR) into microfluidic devices with virtually no limit on channel geometry.[30] Coupling this with an aperture-based scanning system for low-cost chemical mapping[31] opens the door to multi-point measurements for kinetic studies. Moreover, the approach allows the ATR element to be refocused as a sensor, boosting signal quality, rather than dedicating valuable surface area to world-to-chip connectors and mixers. With this capability, microfluidics and FTIR spectroscopy for *in situ* measurements can be an accessible route to study nearly any chemical reaction, including those with highly reactive intermediates and complex reaction pathways.

In this work, we demonstrate a proof-of-concept spectIR-fluidic reactor design for kinetic studies fast reactions. We use a nearly instantaneous protonation reaction of a buffer molecule to benchmark key figures of merit and related to time resolution and the first time point after mixing. Using our device, we demonstrate that the reaction proceeded to 94 % within 28 ms and reached equilibrium after 130 ms. With this upper limit on reaction speed determined, this work opens the door to a wide range of reactions, which that can benefit from full-spectrum characterization by ATR-FTIR for simultaneous quantification of reagents, intermediates and products. The method also provides a method for systematically determining performance of microfluidic mixing elements under different flow conditions.

Experimental

The spectroscopy enhanced microfluidic device (herein referred to as a "spectIR-fluidic device") was prepared by plasma bonding the microchannel layers and ATR sensing layer, as recently shown.[29] The microchannel layer was fabricated using polydimethylsiloxane (PDMS) (Sylgard184, Dow, Canada) mixed with a cross-linking agent at a 10:1 ratio, which was cast against a mould. The reaction device mould was fabricated by photolithography using a laminate photoresist with 50 µm thickness (SF4000, Mungolux, Germany) adhered to glass (75 x 50 mm, Fisherbrand™ Plain Glass Microslides, Fisher Scientific, USA). The channel geometries were designed by computer-aided design software (AutoCAD, Autodesk, USA). The ATR sensing layer featured a multi-ridge ATR crystal (Basic Universal, IRUBIS GmbH, Germany) that were used without further modifications. The ATR crystal dimension was 11 mm by 9 mm, but this included a 1 mm boarder around its edge, which does not feature ridges on the bottom side, and therefore, is not couple to the probe light on it sample detection side. Therefore, the sensing region only measured 9 mm by 7 mm. To prepare the ATR crystal layer, it was placed on top of a flat substrate with the sensing surface facing down. The PDMS mixture solution was then poured over the crystal to immerse it. After curing, the ATR crystal layer was ready for plasma bonding. For further details, the reader is referred elsewhere.[30]

The test analyte used in this study were sodium phosphate dibasic (Na_2HPO_4) (84486-300, Anachemia, Canada), which is a major component of the popular biological sodium phosphate buffer. A stock solution of 0.2 M was prepared by dissolving 2.84 g of Na_2HPO_4 in 100 mL of deionized water. Hydrochloric acid (HCl, Fisher Scientific, USA) solution (0.064 M, pH = 1.5) was prepared by adding dropwise to a stirred container while monitoring pH using a pH meter (AB150 pH Benchtop Meters, Fisher Scientific, USA). Fast reaction studies of the buffer protonation kinetics were undertaken by on-chip mixing of the HCl and Na_2HPO_4 solutions. The prepared solutions were delivered to the spectIR-fluidic device through world-to-chip inlets in the device via conduit 1.6 mm outer diameter perfluoroalkoxy (PFA) tubing (U-1148, IDEX, WA, USA). At their upstream side, each conduit was connected to a 10 mL syringe (BD-General Use-30mL, Fisher Scientific, Canada) with a threaded connector assembly (P-200x, P-658, IDEX, WA, USA). Flow rate was controlled by a separate syringe pump for each solution (NE 1000X, New Era, USA).

https://doi.org/10.26434/chemrxiv-2023-jd51z ORCID: https://orcid.org/0000-0002-0880-9782

SpectIR-fluidic devices were mounted on a custom ATR spectroscopy microfluidic assay accessory (ASMAA) that was designed to operate with the multiridge Si-ATR crystals used in this work. The system featured a moving aperture with slit width of 0.7 mm, which selectively coupled light to different locations on-chip with the aid of a computer-controlled moving aperture. For more details on the ASMAA systems, the reader is referred to a previously demonstrated system.[31] Measurements were acquired with a research-grade spectrometer (Invenio R, Bruker Ltd. Canada), which was placed on an anti-vibration table. The detector was a nitrogen-cooled MCT variant and the spectrometer system was controlled by computer software (OPUS, Bruker, USA). The beam splitter used was KBr, and during the tests, a purge gas generator was used to limit atmospheric interference. To obtain the spectra, 64 co-additions were taken with a scan velocity of 1.27 cm s^{-1} (10 kHz) and a spectral resolution of 4 cm^{-1}.

Computational fluid dynamics simulations (COMSOL Multiphysics V5.4, Stockholm, Sweden) were used to determine the flow velocities and concentration profiles under steady state conditions. This was achieved with laminar flow and transport of diluted species modules and a Navier-slip boundary condition at the channel walls. Diffusion coefficients of D_{HPO4^-} = 0.69×10^{-9} m^2 s^{-1} and D_{H^+} = 9.31×10^{-9} m^2 s^{-1} were used for phosphate and hydrogen ions, respectively. Liquids were treated as incompressible Newtonian fluids under isothermal laminar flow conditions. An initial triangular mesh was built with a total of 52006 elements, covering the entirety of the geometry (total of 51.65 mm^2). The COMSOL adaptive mesh functionality was used, and the mesh was refined selectively using an error function (L_2 norm of the error, defined by

$$L_2 = \sqrt{\sum_{i=1}^{N}\left(y_i - y_i^{pred}\right)^2} \qquad (1)$$

where y and y^{pred} represent each data from each refining step (from i=1 to N) and the ones from the previous mesh). The number of elements was increased by 70% at each step, with a total of 6 iterations performed. The final mesh obtained contained 1101086 elements. A PARDISO numerical solver was used to solve the system, and the relative tolerance for the convergence criteria value was 0.001. Single ray path simulations were run to predict the light path through the ATR ridges. The simulation was based on first principles, including Snell's law and geometrical optics considerations as explained previously.[31] Further details can be found in the Electronic Supplementary Information (ESI).

Results

One of the principle advantages of the spectIR-fluidic fabrication approach was the ability to include arbitrary complexity in the reactor design and world-to-chip interfacing, without sacrificing ATR crystal sensing surface area to serve a dual role as device chassis. We took advantage of this capability by placing non-analytical microfluidic features (world-to-chip connections and mixer) away from the ATR crystal. We designed and implemented a two-inlet/one-outlet spectIR-fluidic device with a series of analytical switchbacks which occupied the entirety of the ATR sensor region progress of chemical reactions could be monitored (Figure 1a). One advantage of this fabrication approach is that the sealing surfaces are either PDMS/PDMS or PDMS/Si, both of which provide strong, leak-proof bonding. This is especially important in the analytical switchback channels on top of the Si-ATR crystal, in order to ensure that liquid does not pool in dead spots nor does it short-circuit the flow path, as either would render the required distance to time calculation impossible. To better visualise the channels of the real spectIR-fluidic device and to test its leak-proof bonding a red dye solution was injected and flowed overnight (5 mL h^{-1}). Following this test, we acquired an image of the device (Figure 1b). A continuous scan across the ATR revealed no water bands, thus confirming the leak-proof operation of the device. In Figure 1b, the ridge side of the ATR crystal is shown to help indicate the placement of the ridges relative to the analytical switchback channels.

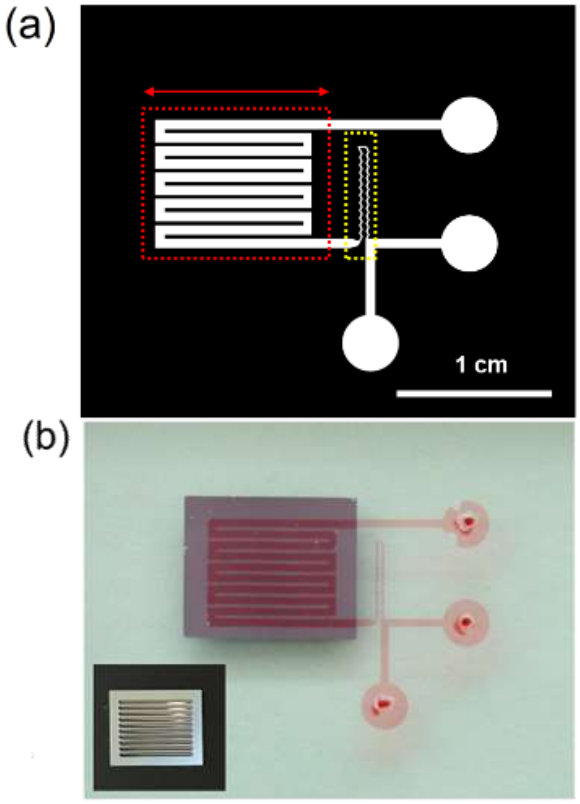

Figure 1. (a) Schematic image of reactor device with 100 µm mixing channels and 0.5 mm reactor switchback channels (red dashed) and mixing element (yellow dashed). (b) Image of a reactor device after 24 hours under 5 mL h^{-1} with channels containing red dye to enhance contrast and an inserted image provides bottom view of an ATR crystal.

We used the largest aperture possible (0.7 mm) which matched the ATR ridge width of the same size. This ensured that the entire ATR ridge was illuminated, thus maximising the amount of light admitted to the corresponding analytical switchback channel. We simulated the light path through the ATR ridge and determined that the corresponding width of the measurement

zone at the ATR sampling surface was 0.46 mm, equivalent to 92% of the total switchback channel width (0.5 mm).[31] Ensuring that nearly the entire analytical switchback channel is monitored nearly eliminates any measurement bias that could occur from an measurement that were not perfectly centred along the channel mid-point. As a reference, the light path using an aperture of only 0.5 mm, resulting in measurement zone of only 0.20 mm wide (Figure 2a), is compared to the 0.7 mm aperture used in this work (Figure 2b). The switchback design yields a 10 parallel flow paths, the first 9 of which were coupled to separate ATR ridges. Thus, every ATR ridge was utilized to maximize the usable sensing surface on the ATR crystal. Alignment between the ridges and switchback channels was achieved using guide marks to align the bonding.

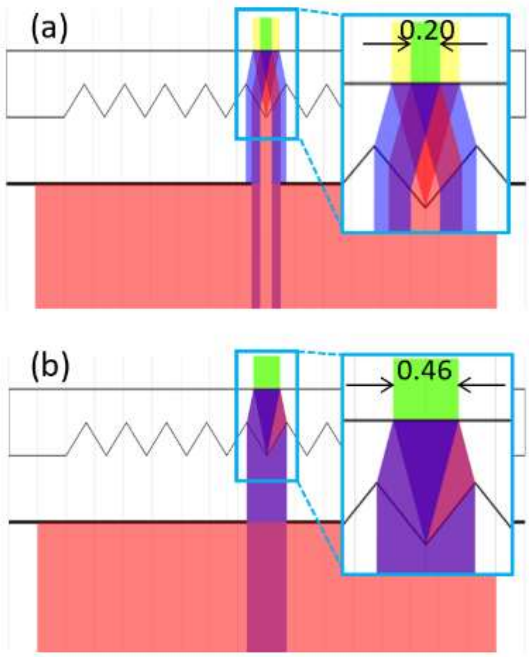

Figure 2. Light path simulation through the ATR crystal, showing the cross-section of the ATR (white, with the ridges at the bottom) light entering from the bottom (pink) and passing through an aperture. Light is coupled into a ridge creating an illumination zone at the sample surface before being reflected backward (purple). Light reaching the illumination zone that is blocked on by the aperture on the way out results in an un-detectable evanescent field (yellow), whereas light that is transmitted through the aperture on the way out produces a detectable evanescent (green), which constitutes the measurement zone. The height of the evanescent field is not to scale. (a) An example of a narrow aperture (0.5 mm) that blocks some light from leaving the aperture and has a narrow measurement zone width (0.2 mm). (b) An example of a wide aperture (0.7 mm) that allows all light to leave the aperture and has a wide measurement zone width (0.46 mm). Insets show zoom view of the ATR crystal and sensing surface, including measurements of the width of the latter.

As a proof-of-principle, we chose a simple mixer design consisting of narrow zigzag channels. An important goal in designing the mixing compartment was to minimize the hydraulic retention time so that the mixed solution could be rapidly injected into the reaction monitoring compartment to enable the start of measurements at early reaction times; however, this should be balanced with sufficient mixing capacity. Therefore, in this work, we fabricated the mixing compartment with a reduced channel volume of only 60 nL (based on a width of 100 μm and height of 50 mm) and then determined the maximum flow rate that could support full mixing before the first measurement location. Optimized mixer designs can be implemented to achieve the faster mixing required for fast reactions, but they are not considered here. Based on the volumes of different features in the spectrofluidic device (analytical switchback channels measuring 0.5 mm in width and 0.9 mm in length) and mixer unit to obtain hydraulic retention times. Based on the exact volumes of each portion of the device, we ran computational fluid dynamic simulations to obtain the hydraulic retention times through each feature. We simulated hydrodynamic conditions using a refined mesh as shown in Figure 3a. See the experimental section and the Supporting Information for more details. In Figure 3b we simulated the velocity profile throughout the channels under steady-state conditions. The individual reactor switchback channels shown in Figure 3c were used to calculate hydraulic retention times for each feature, with the result being tabulated in Table 1. The results from simulations produced similar results to those from a simple calculation of hydraulic retention time (t_h) based on Equation 2.

$$t_h = d_{ATR}/u = V_{ATR}/Q \quad (2)$$

where t_h is in seconds, the distance corresponding to the active portion of the crystal along the downstream direction (d_{ATR}) is 7 mm, the channel volume along the active portion of the ATR crystal (V) is 9.45 μL for a typical switchback channel, and the volumetric flow rate (Q) is in μL s^{-1}.

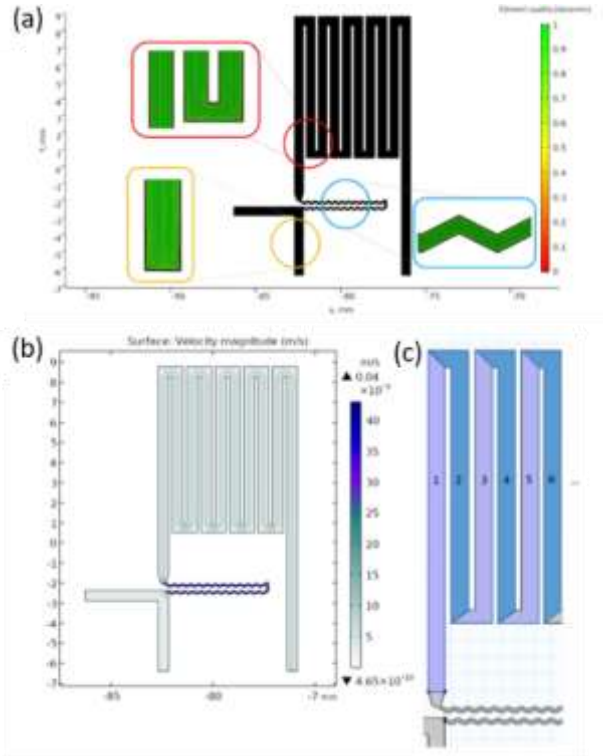

Figure 3. (a) Figure showing model area and mesh density with highlights on the inlet junction (yellow), mixing region (blue) and reaction switchback channels (red). The colour bar correlates to the quality of elements (generally green, high quality). Refined (b) Velocity profile (m s^{-1}) across the geometry. (c) Schematic image shows the division of the switchback channel.

Table 1. Convective flow details for a reactor device.

Feature	Volume	Volume*	$Time_1$**	$Time_2$**
	(nL)	(μL)	(ms)	(ms)
Mixer	60	0.06	13.39	60
Channel 1	252	0.127	28.18	126.27
Channel 2	466	0.359	80.13	359.04
Channel 3	679	0.572	127.72	572.27
Channel 4	892	0.786	175.31	785.5
Channel 5	1105	0.999	222.90	998.73
Channel 6	1319	1.212	270.49	1211.96
Channel 7	1532	1.425	318.08	1425.19
Channel 8	1745	1.638	365.67	1638.42
Channel 9	1958	1.852	413.27	1851.65
Channel 10	2172	2.065	460.86	2064.88

* Reports the volume and time, which are the cumulative values after mixing until the midpoint of the channel in question, except for the mixer channel, which reports its entire volume/time.

** Hydrodynamic retention times $Time_1$ and $Time_2$ are calculated based on total flow rates of Q_T=16 mL h^{-1} and Q_T=1.3 mL h^{-1}, respectively.

We monitored the evolution of the reaction mixture as it flowed through the device by moving the aperture to different ATR ridges and recording spectra. This resulted in the illumination of an entire switchback channel length, producing one measurement representing the average reaction state at the midpoint position. It is important to note that recent work has demonstrated that the resulting surface measurements using ATR gives concentrations that are representative of the bulk fluid for low-aspect ratio channels (height to width),[32] which is not obvious considering that no-slip conditions at the channel surface results in slower flow rates (and longer reaction times) compared to the bulk liquid. The maximum observable reaction time was based on the hydraulic retention time within the volume between the beginning of the first switchback channel and the middle position of the last (ninth) ridge-coupled switchback channel (1960 nL).

In this work, we used a nearly instantaneous reaction between the sodium phosphate dibasic buffer molecule and a pH 1.5 HCl solution to determine the maximum flow rate that could achieve full mixing by the first switchback channel. To begin, each reagent was flowed at 8 mL h^{-1} (Q_T=16 mL h^{-1}). This fast flow rate, combined with the relatively modest mixer, was assumed to not provide adequate time for complete mixing, which was expected to reveal itself as residual changes to the reaction system as remaining concentration gradients caused the buffer molecules to diffuse throughout the channel and finished neutralizing the residual protons from the HCl stream. The flow velocity (u) can be calculated using Equation 3:

$$u = Q/A \quad (3)$$

where u is in mm s^{-1}, the flow rate (Q) is in μL s^{-1}, and the channel cross-section area (A) is in mm^2. We calculated a fluid velocity of 176 mm s^{-1} based on the total volumetric flow rate (Q_T=16 mL h^{-1}) and the channel cross-sectional area (0.025 mm^2). This is approximately the same velocity as was calculated along the channel centre-plane from our computational fluid dynamics simulations (Figure 3a). Using the reactor volume from the beginning of the mixing channel until the midpoint of the ninth switchback in Equation 1, the maximum observable reaction time was 413 ms, whereas coupling the IR probe light to the first ridge/channel location obtained the state of the reaction at an earlier time, as low as 28 ms.

Before the experiment, we recorded 9 absorbance spectra (off-chip) from sodium phosphate dibasic ([Na_2HPO_4] = 0.1 M) with pH adjusted between 1.5 and 9. The resulting spectra shown in Figure 4a present a number of peaks that originate from the various phosphate protonation states.

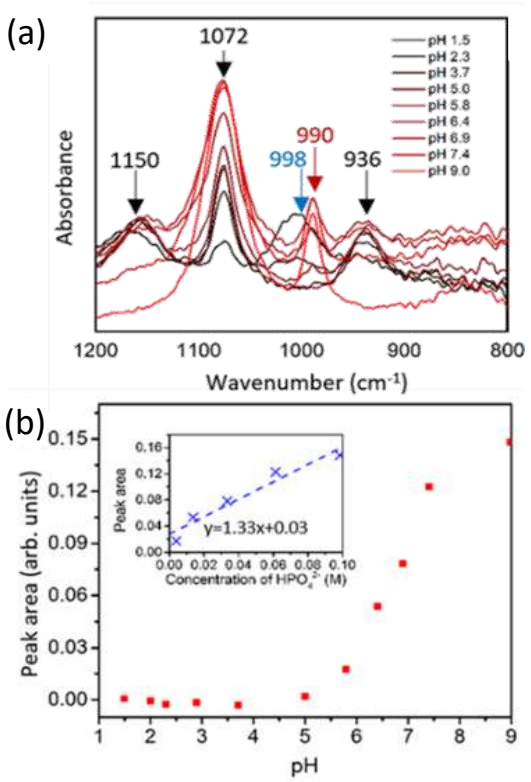

Figure 4. (a) Stacked absorption spectra with changing pH. (b) Area of peak intensity at 990 cm^{-1} of the phosphate molecule in different pH environments. Inset shows the calibration curve of the integration values *vs.* different concentrations of HPO_4^{2-}.

The conversions between different protonated states and their equilibrium constants are given in Equations 4 to 6.[33]

$$H_3PO_4 + H_2O \rightleftharpoons H_3O^+ + H_2PO_4^- \qquad K_{a1} = 7.11 \times 10^{-3} \quad (4)$$

$$H_2PO_4^- + H_2O \rightleftharpoons H_3O^+ + HPO_4^{2-} \qquad K_{a2} = 6.32 \times 10^{-8} \quad (5)$$

$$HPO_4^{2-} + H_2O \rightleftharpoons H_3O^+ + PO_4^{3-} \qquad K_{a3} = 4.49 \times 10^{-13} \qquad (6)$$

To summarize based on the literature, one peak was observed at 998 cm^{-1} at very low pH values, corresponded to H_3PO_4 and the three other peaks at 1150, 1072 and 936 cm^{-1} arose from $H_2PO_4^-$.[34] Although these peaks were observed over a wide range of pH values owing to their intermediate protonation state between HPO_4^{2-} and H_3PO_4, their pH-dependent intensities vary independently of each other, making quantification of the degree of reaction difficult. Lastly, at high pH, a band at 990 cm^{-1} appeared at pH > 5, which corresponded to the intermediate protonation state of HPO_4^{2-}. A plot of the vibrational peak area of this band as a function of pH confirms a nearly linear increase in absorbance between pH 5 to 7.5 (Figure 4b). The HPO_4^2 band intensity at 990 cm^{-1} continued to grow up to pH 9, but at a less pronounced rate and with a different trend. Therefore, we used the band at 990 cm^{-1} as an indicator of $[HPO_4^{2-}]$, within an acceptable pH range. The $[H_3PO_4]$, $[H_2PO_4^-]$, and $[PO_4^{3-}]$ in this solution system are related to $[HPO_4^{2-}]$, and can be calculated using Equations 7 to 9:

$$[H_3PO_4] = \frac{[HPO_4^{2-}][H^+]^2}{K_{a1}K_{a2}} \qquad (7)$$

$$[H_2PO_4^-] = \frac{[HPO_4^{2-}][H^+]}{K_{a2}} \qquad (8)$$

$$[PO_4^{3-}] = \frac{[HPO_4^{2-}]K_{a3}}{[H^+]} \qquad (9)$$

Since the initial concentration of HPO_4^{2-} was 0.1 M, the summation of concentration of all phosphate ions must remain constant at 0.1 M (Equation 10):

$$[H_3PO_4] + [H_2PO_4^-] + [HPO_4^{2-}] + [PO_4^{3-}] = 0.1\ (M) \qquad (10)$$

By combining Equations 7 to 9 with Equation 10, we could obtain the relation between $[HPO_4^{2-}]$ and $[H^+]$:

$$[HPO_4^{2-}] = \frac{0.1 \times [H^+]K_{a1}K_{a2}}{[H^+]^3 + [H^+]^2K_{a1} + [H^+]K_{a1}K_{a2} + K_{a1}K_{a2}K_{a3}} \qquad (11)$$

As the $[H^+]$ could be obtained from the solution pH, all phosphate group concentrations at different pH can be calculated (see Table 2).

Table 2. Concentration calculations of phosphate protonation states at different pH values

pH	$[PO_4^{3-}]$ (M)	$[HPO_4^{2-}]$(M)	$[H_2PO_4^-]$(M)	$[H_3PO_4]$ (M)
1.5	5.04 x 10^{-19}	3.59 x 10^{-8}	0.018179	0.08182
2.3	6.66 x 10^{-17}	7.42 x 10^{-7}	0.058711	0.041288
3.7	6.9 x 10^{-14}	3.07 x 10^{-5}	0.097234	0.002735
5	2.82 x 10^{-11}	0.000627	0.099233	0.00014
5.8	1.09 x 10^{-9}	0.003845	0.096133	2.14 x 10^{-5}
6.4	1.55 x 10^{-8}	0.013703	0.086292	4.83 x 10^{-6}
6.9	1.19 x 10^{-7}	0.033403	0.066595	1.18 x 10^{-6}
7.4	6.92 x 10^{-7}	0.061359	0.03864	2.16 x 10^{-7}
9	4.42 x 10^{-5}	0.098399	0.001557	2.19 x 10^{-7}

We combined the calculated the pH-based HPO_4^{2-} concentration with the measured pH-dependant HPO_4^{2-} peak area (at 990 cm^{-1}) to obtain a calibration curve (Figure 4b inset). Next, we flowed water at pH 9.2 through the device and obtained background (single-beam) spectra from each switchback channel. We subsequently flowed an HCl solution (Q=8 mL h^{-1}, 0.128 mol L^{-1}, pH=0.9) to inlet 1 and a HPO_4^{2-} solution (Q=8 mol L^{-1}, 0.2 M, pH=9.2) to inlet 2. The concentration of the latter was twice that of the maximum range for our calibration curve (Figure 4b inset) to account for the diluting effect of the co-flowing reagent after mixing. The effect of protonation was expected to further reduce $[HPO_4^{2-}]$. Based on the dilution of the HPO_4^{2-} and HCl streams (to 0.100 M and 0.064 M, respectively) and the subsequent protonation of the neutralization strong acid HCl, $[HPO_4^{2-}]$ is expected to reach approximately 0.036 M at the end of the reaction. We obtained spectra from all 9 switchback channels (Figure 5a) and integrated the band at 990 cm^{-1} to obtain its peak area. After using a reference method to ensure comparable absorbance values across the sensing surface,[31] we used the calibration curve in Figure 4 as a universal approach to obtain the concentrations in any channel. We confirmed these measurements with a second approach in which the percent reduction of peak areas in each channel during protonation were compared to the peak area of a 0.1 M HPO_4^{2-} solution, which yielded the same results. As shown by the results in Figure 5b, after the first measurement zone, the concentration had become significantly reduced from the initial (diluted) concentration of 0.1 M to nearly 0.04 M. This constitutes a reaction completion of 94%, considering the predicted final concentration of 0.036 M. As the reaction of the buffer molecule with protons should be nearly instantaneous in a fully mixed reaction solution, the completion to less than 100% after this tells us that there the mixing is not complete after 28 ms (see Table 1). The decrease in the peak area continued until the third reactor switchback channel, at which time (130 ms) the diffusion-limited reaction process was complete with the final concentration very close to the predicted final concentration of $[HPO_4^{2-}]_f$=0.036 M. From these results, we determined that the total flow rate should be reduced to Q_T=1.3 mL h^{-1} to increase the initial time point to 128 ms to ensure that mixing is complete before the first measurement (Table 1). Under these flow condition, the reaction state was complete and stable between the first and last measurement position (Figure 5b).

The presented method can approximate the optimal operational conditions and the resulting timing of kinetic measurements for any design. Future designs with improved mixer dimemsions or even mixer types can be implemented and benchmarked using the same method.

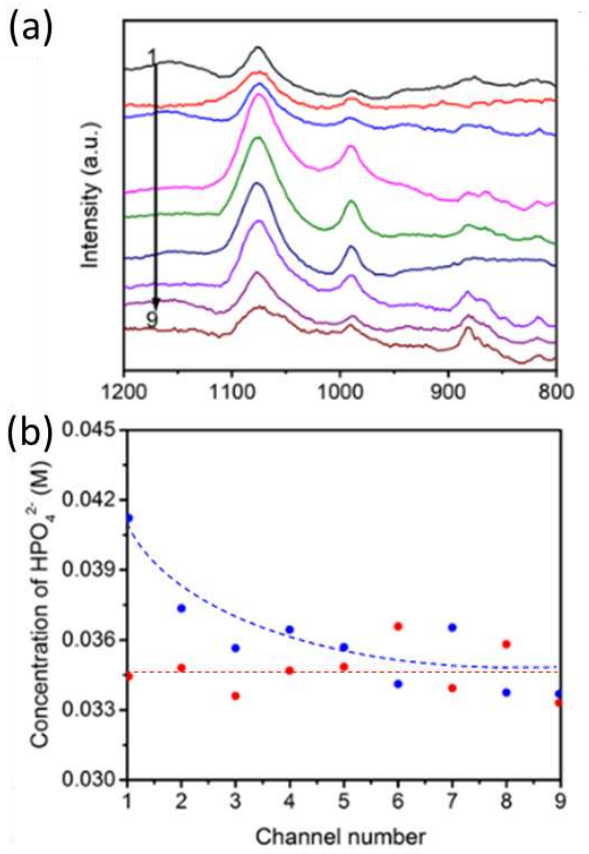

Figure 5. (a) Stacked absorption spectra obtained from each channel during the reaction. Spectra from top to bottom correspond to channel 1 through channel 9. (b) Calculated concentration of HPO_4^{2-} in channel 1 to channel 9 using the integration values of peak intensity at 990 cm^{-1} at a total flow rate of Q_T = 16 mL h^{-1} (blue) and Q_T=1.3 mL h^{-1} (red). Dashed lines are for eye guidance.

Discussion

The results above validate the use of a "spectIR-fluidic" sensing platform as a tool for chemical kinetic studies in microchannels using FTIR. The benefit of conducting multi-point *in situ* measurements, as is demonstrated here, is that reaction time points can be obtained while flow rate and mixing remain constant. Also, data acquisition time can be arbitrarily long without impacting the time resolution of the kinetic study. At a total flow rate of 16 mL h^{-1}, we showed that approximately 130 ms was sufficient to achieve full mixing of the reaction system. At the corresponding flow rate, time resolution between measurements in different switchback channels was 50 ms. In this proof-of-principal study, a simple saw-tooth mixer was employed, but applying more efficient mixers[35] would enable faster flow rates. In turn, this would improve the time resolution. For example, a mixer capable of achieving full mixing after 1 ms, would enable increase to flow rates of approximately 30 times, corresponding to a time resolution of under 2 ms. In addition to flow rate modification, the complete customizability of the spectIR-fluidic reactor design can be exploited to further increase the range of applicable reaction times. This could be exploited with designs that produce shorter hydraulic retention times in each switchback channel for better time resolution, such as by reducing channel heights. At the limit, channel height could be reduced to match the evanescent field penetration depth (*ca.* 1 µm) without affecting data quality. As such, flowing at the same 16 mL h^{-1} used in this work, would lead to a time resolution near 1 ms. It should be noted that we have validated that the current system can be safely operated under total flow rates of at least 40 mL h^{-1} (the upper limit in flow rate was not found in these tests), but that validation tests of leak-proof operation should be verified under new channel dimensions since shear stress increases with the square of the channel height. An approach to increasing time resolution without any changes to channel dimensions or applied flow rates is to monitor sub-domains within each switchback channel using a 2D scanning approach. While such a system has not yet been demonstrated, preliminary tests in our lab demonstrate that smaller aperture that would be required will generate lower signals. However, this may be offset by the integration of multi-ridge Si-ATR crystals with surface-enhanced IR capacity.[36] Among the various routes to accommodate slow reactions, the most obvious is to maintain channel design, while increasing channel heights. Additionally, flow paths can also be significantly elongated thanks to the completely seamless integration of the Si-ATR into the PDMS device, thus enabling flow channels to repeatedly cross between ATR-PDMS and full PDMS channels. We calculate that 500 µm-tall channels occupying 80% of the area of a credit card-sized reactor device (accounting for walls between channels that occupy 20% of the available area) could support kinetic studies with total reaction monitoring time of 20 hours at a volumetric flow rate of 0.1 mL h^{-1}. It is also noted that for slow reactions simpler (and slower) mixers can be employed. We note that the high transparency in the visible spectral window, can be exploited for FTIR studies of photo-chemical reactions, and that the excellent thermal diffusion in microchannels can enable reactions at precise temperatures, including studies of activation energy barriers via the Arrhenius plot methodology. Finally, we note the fundamental limitation that remains in this approach is the limited chemical compatibility between the PDMS device and solvents used in chemical synthesis.[37] Future approaches to incorporate the Si-ATR into other materials should be investigated to address this issue.

Conclusions

This study will contribute to the field of microfluidics and chemical analysis by introducing a new device for multi-point *in situ* measurements by FTIR. The system was used to validate mixing times using an optimized mixer applied to a fast protonation reaction and analytical details, such as time resolution were determined. The tool is robust and can be optimized for fast or slow reactions based on proposed changes to device design and experimental conditions. Thus, the approach has the distinct potential to provide valuable insights into the reaction kinetics and mechanisms of a wide range of chemical reactions. The spectIR-fluidic reactor has the potential

to accelerate the development of new chemical reactions and reaction pathways by providing real-time data on the reactions. Additionally, the device has the potential to enable the optimization of reaction conditions and parameters for improved reaction yield, selectivity, and efficiency.

Author Contributions

Nan Jia: outline generation, writing - original draft, table and figure generation, data curation, formal analysis. Leon Torres de Oliveira: simulations. André Bégin-Drolet: supervision, project administration, methodology, editing. Jesse Greener: conceptualization, funding acquisition, methodology, project administration, resources, supervision, visualization, writing – review and editing.

Conflicts of interest

There are no conflicts to declare.

Acknowledgements

The authors wish to thank The Natural Sciences and Engineering Research Council of Canada for funding, Genome Canada/Quebec for instrumentation, and Molly K. Gregas for technical editing.

References

1 (a) D. J. Beebe, G. A. Mensing G. M. Walker, *Annu. Rev. Biomed. Eng.*, 2002, **4**, 261-286; (b) K-i. Ohno, K. Tachikawa, A. Manz, *Electrophor*., 2008, **29**, 4443-4453; (c) A. F. Oliveira, A. C. S. N. Pessoa, R. G. Bastos, L. G. de la Torre, *Biotechnol. Prog*., 2016, **32**, 1372-1389; (d) M. P. C. Marques, N. Szita, *Curr. Opin. Chem. Eng.*, 2017, **18**, 61-68.

2 (a) P. Mesquita, L. Gong, Y. Lin, *Front. Lab. Chip. Technol.*, 2022, 1074009; (b) P. Pattanayak, S. K. Singh, M. Gulati, S. Vishwas, B. Kapoor, D. K. Chellappan, K. Anand, G. Gupta, N. K. Jha, P. K. Gupta, P. Prasher, K. Dua, H. Dureja, D. Kumar, V. Kumar, *Microfluid. Nanofluidics*, 2021, **25**, 99; (c) J. Greener, in Functional Materials: For Energy, Sustainable Development and Biomedical Sciences, De Gruyter, Berlin, 2014, 375-414.

3 L. A. Low, C. Mummery, B. R. Berridge, C. P. Austin, D. A. Tagle, *Nat. Rev. Drug Discov.*, 2021, **20**, 345-361.

4 G. Pasirayi, V. Auger, S. M. Scott, P. K. S. M. Rahman, M. Islam, L. O`Hare, Z. Ali, *Micro Nanosyst.*, 2011, **3**, 137-160.

5 (a) M. Pousti, M. P. Zarabadi, M. A. Amirdehi, F. Paquet-Mercier, J. Greener, *Analyst*, 2019, **144**, 68-86; (b) S. F. Berlanda, M. Breitfeld, C. L. Dietsche, P. S. Dittrich, *Anal. Chem.*, 2021, **93**, 311-331.

6 (a) S. Sachdeva, R. W. Davis, A. K. Saha, *Front. Bioeng. Biotechnol.*, 2020, **8**, 602659; (b) C. Dincer, R. Bruch, A. Kling, P. S. Dittrich, G. A. Urban, Trends Biotechnol., 2017, 35, 728-742.

7 J. M. Cooper, *Front. Lab. Chip. Technol.*, 2022, **1**, 979398.

8 H. Song, J. D. Tice, R. F. Ismagilov, *Angew. Chem. Int. Ed.*, 2003, **115**, 792-796.

9 A. D. Radadia, in Encyclopedia of Microfluidics, Nanofluidics. Springer, Boston, 2008, 1195-1207.

10 (a) D. Voicu, C. Scholl, W. Li, D. Jagadeesan, I. Nasimova, J. Greener, E. Kumacheva, *Macromolecules*, 2012, **45**, 4469-4475; (b) M. P. Zarabadi, M. Couture, S. J. Charette, J. Greener, *ChemElectroChem*, 2019, **6**, 2715-2718.

11 H. Song, D. L. Chen, R. F. Ismagilov, *Angew. Chem. Int. Ed.*, 2006, **45**, 7336-7356.

12 A. J. de Mello, *Nature*, 2006, **442**, 394-402.

13 J. K. Lee, S. Kim, H. G. Nam, R. N. Zare, *Proc. Natl. Acad. Sci. U.S.A.*, 2015, **112**, 3898-3903.

14 M. U. Kopp, A. J. de Mello, A. Manz., *Science*, 1998, **280**, 1046-1048.

15 J. P. McMullen, K. F. Jensen, *Org. Process Res. Dev.*, 2011, **15**, 398-407.

16 D. Resetca, D. J. Wilson, *Int. J. Mass Spectrom.*, 2017, **420**, 67-73.

17 X. Duan, J. Tu, A. R. Teixeira, L. Sang, K. F. Jensen, J. Zhang, *React. Chem. Eng.*, 2020, **5**, 1751-1758.

18 Z. Yan, J. Tian, C. Du, J. Deng, G. Luo, *Chin. J. Chem. Eng.*, 2022, **41**, 49-72.

19 J. Wu, G. Zheng, L. M. Lee, *Lab Chip*, 2012, **12,** 3566-3575.

20 H. Song, J. D. Tice, R. F. Ismagilov, *Angew. Chem. Int. Ed.*, 2003, **42**, 768-772.

21 W. Li, K. Liu, R. Simms, J. Greener, D. Jagadeesan, S. Pinto, A. Günther, E. Kumacheva, *J. Am. Chem. Soc.*, 2012, **134**, 3127-3132.

22 G. H. Seong, J. Heo, R. M. Crooks, *Anal. Chem.*, 2003, **75**, 3161-3167.

23 M-E. Mäeots, B. Lee, A. Nans, S-G. Jeong, M. M. N. Esfahani, S. Ding, D. J. Smith, C-S. Lee, S. S. Lee, M. Peter, R. I. Enchev, *Nat. Commun.*, 2020, **11**, 3465.

24 P. R. Griffiths, J. A. de Haseth, Fourier transform infrared spectrometry, Wiley-Interscience, New York, 2nd edn., 2007.

25 A. Pintar, J. Batista, J. Levec, *Analyst*, 2002, **127**, 1535-1540.

26 M. V. Barich, A. T. Krummel, *Anal. Chem.*, 2013, **85**, 10000-10003.

27 (a) H-Y. N. Holman, R. Miles, Z. Hao, E. Wozei, L. M. Anderson, H. Yang, *Anal. Chem.*, 2009, **81**, 8564-8570. (b) M. Pousti, M. Joly, P. Roberge, M.A. Abbaszadeh, A. Begin-Drolet, J. Greener, Linear scanning ATR-FTIR for chemical mapping and high-throughput studies of Pseudomonas sp. biofilms in microfluidic channels, *Anal. Chem.*, 2018, **90** (24), 14475–14483

28 J. Greener, B. Abbasi, E. Kumacheva, *Lab Chip*, 2010, **10**, 1561-1566.

29 (a) K. L. A. Chan, X. Niu, A. J. de Mello, S. G. Kazarian, *Lab Chip*, 2010, **10**, 2170-2174; (b) T. A. Morhart, S. T. Read, G. Wells, M. Jacobs, S. M. Rosendahl, S. Achenbach, I. J. Burgess, *Anal. Methods*, 2019, **11**, 5776-5783.

30 N. Jia, A. Daignault-Bouchard, T. Deng, T. G. Mayerhöfer, A. Bégin-Drolet, J. Greener, *Lab Chip*, 2023, submitted.

31 M. Joly, T. Deng, T. A. Morhart, G. Wells, S. Achenbach, A. Bégin-Drolet, J. Greener, *Anal. Chem.*, 2021, **93**, 14076-14087.

32 G. T. Flaman, N. D. Boyle, C. Vermelle, T. A. Morhart, B. Ramaswami, S. Read, S. M. Rosendahl, G. Wells, L. P. Newman, N. Atkinson, S. Achenbach, I. J. Burgess, *Anal. Chem*., 2023, **95**, 4940-4949.

33 (a) J. Bjerrum, G. Schwarzenbach, L. G. Sillén, The Chemical Society, London, 1957; (b) G. Falcon-Millan, M.P. Gonzalez-Muñoz, A. Durand, J. A. Reyes-Aguiler, T. A. Razo-Lazcano, M. Avila-Rodriguez. *J. Mol. Liq.*, 2017, **241**, 967-973.

34 E. J. Elzinga, D. L. Sparks, J. *Colloid Interface Sci.*, 2007, **308**, 53-70.

35 (a) C.-Y. Lee, W.-T. Wang, C.-C. Liu, Lung-Ming Fu, *Chem. Eng. J.*, **288**, 2016, 146-160. (b) C. Y. Lee, C. L. Chang, Y. N. Wang, L. M. Fu, *Int. J. Mol. Sci*. 2011, **12**(5), 3263-87.

36 T. A. Morhart, B. Unni, M. J. Lardner, I. J. Burgess, *Anal. Chem.*, 2017, **89**, 11818-11824. (b) J. Haas, A. Müller, L. Sykora, B. Mizaikoff, *Analyst*, 2019, **144**, 3398-3404 (c) I. L. Jernelv, J. Høvik, D. R. Hjelme, A. Aksnes, *Proc. SPIE* 11359, Biomedical

Spectroscopy, Microscopy, and Imaging, 113590A (1 April 2020);
37 J. Ng Lee, C. Park, G. M. Whitesides, *Anal. Chem*., 2003, **75**, 23, 6544–6554